

Non-Linear Dynamic Modeling of Cartesian-Frame FFF 3-D Printer Gantry for Predictive Control

Maharshi A. Sharma¹ and Albert E. Patterson^{1,2}

¹Department of Mechanical Engineering, Texas A&M University, College Station, TX 77843

²Manufacturing and Mechanical Engineering Technology, Department of Engineering Technology and Industrial Distribution, Texas A&M University, College Station, TX, 77843

maharshiarindom@tamu.edu; aepatterson5@tamu.edu

Abstract

This paper presents the development of a dynamic model of an FFF 3-D printer gantry (2-D) that is useful for developing an open-loop predictive control system. This predictive control system based on the mechanics of the system will help to reduce manufacturing defects by minimizing position error in the printing head. A six-dimensional non-linear dynamic model of the printer gantry was derived using Newton-Euler method, followed by a Lagrangian dynamic model to gain additional insight on energy transfer aspects and model validation. A state-space model of the full system was developed for positioning and control. A detailed case-study of an example printer was completed in MATLAB-Simulink to demonstrate the system model with comparisons from the analytical model and physical characterization on a real printer. Finally, a few examples of passive control designs were illustrated for predictive control development. It was concluded that dynamics-based predictive control is a promising, realistic, and practical approach to controlling the dynamic error and dimensional error commonly seen with FFF machines.

Keywords: FFF process; extrusion-based additive manufacturing; control systems; dynamic modeling

1. Introduction

Additive manufacturing (AM) technologies have become a fixture in modern manufacturing technology, becoming widely used and removed from the early “rapid prototyping” efforts. The fused filament fabrication (FFF), most commonly known as fused deposition modeling (FDM), process is one of the most widespread and widely recognized. As new uses and industries push the current limits of AM, the inadequacies and disadvantages of the processes become ever more apparent. The cost and effort involved in inventing and developing new processes is massive, so it is far more effective and efficient to attempt to address problems with the currently available processes and improve them.

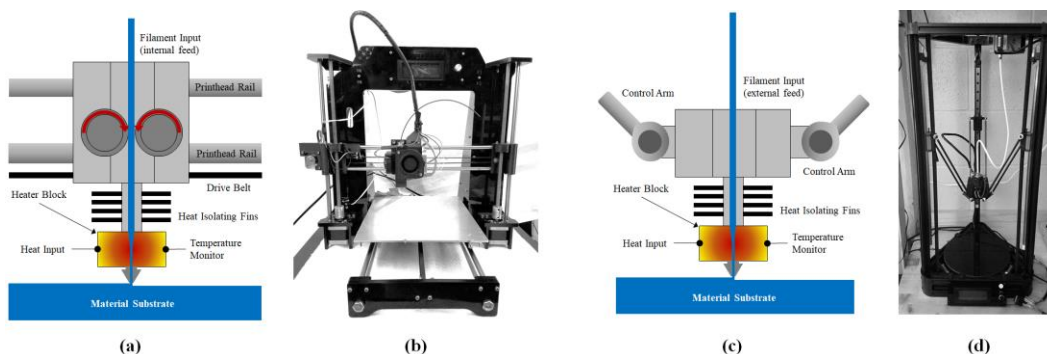


Figure 1: (a-b) Cartesian frame and (c-d) delta-frame printer designs

The FFF systems themselves can be configured in a variety of ways, the only essential mechanical requirement being that the extruder die must be held close to a strong and secure build surface to build the part on. This is typically done using a cartesian-based 3-axis system but is also done using a delta robot configuration [1-4]; multi-axis robotic arms and several other highly specialized systems have been successfully used in the lab, but these are typically considered a different class of manufacturing process and are not available for most applications [5-8]. Figure 1 shows the basic concept for the cartesian (Figure 1a) and delta frame (Figure 1c) configurations. Figure 1b and Figure 1d show full-machine examples of the cartesian and delta printer types, respectively.

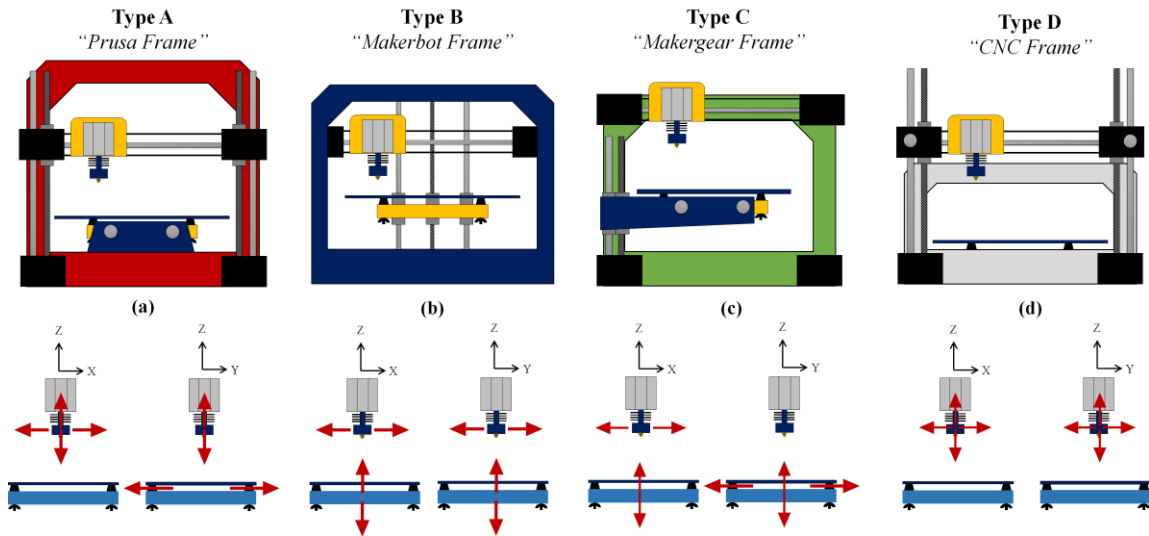


Figure 2: FFF frame classes, (a) Prusa, (b) Makerbot, (c) Makergear, and (d) CNC [16]. Figure reproduced under the terms of a CC-BY license.

The most commonly used 3D printing system by far is the x-y-z frame system. It is more cost-effective, simpler to operate and maintain, and is much more intuitive for most users. It uses linear motion to deposit materials and is the style most often used in polymer AM research. A significant amount of research has been done on the mechanics of delta robots in the past, including several system models [4, 9-15], but very little on the mechanics of cartesian-system printers. For these reasons, the focus of the present study was on the cartesian-frame style of FFF machine. In the world of cartesian-frame FFF machines, four different classes of machines have emerged (Table 1). The classes are defined according to the linear motion of each of the main components within the system, each class having a different system of motion. A representative diagram of the four classes, as well as the coordinate system used on all designs, is shown in Figure 2. A clear understanding of the different types is essential in the correct modeling of the system to be applicable for modeling the extruder carriage motion.

Table 1: FFF machine classes [16]. Reproduced under the terms of a CC-BY license.

Type	Attributes	Figure
A	Commonly known as the <i>Prusa-frame</i> printer, this is by far the most common design of desktop and research lab FFF systems. The print bed is fixed to move only in the y-axis, while the extruder carriage moves in the x-axis and the z-axis. This design allows the fastest printing speed of any of the cartesian-frame printers, is the easiest to use with thin layers (50-100 μ m), and has the lowest sensitivity to filament quality. It is, however, the most subject to part errors caused by system compliance and vibrations.	2a
B	Often known by the brand name of its most well-known member, the <i>Makerbot-frame</i> printers are commonly seen as medium-to-large commercial-grade machines. The print bed motion is restricted in the z-axis (the build direction), while the x-axis and y-axis are covered by the extruder carriage. This design allows a very large build area and simple integration of multiple extrusion nozzles but is typically much slower than Prusa-frame machines (500-1000% in some cases). It is also typically sensitive to filament quality and needs more maintenance between prints due to the “hanging” cantilever build plate.	2b

C	A much less common machine type, it is a combination of Classes A and B. The motion of the extruder carriage is restricted to the x-axis, while the print bed itself moves in the y- and z-axes. Typically, far more compact than Class B machines, this design attempts to combine the advantages of both Class A and Class B but combines most of the disadvantages.	2c
D	This design uses the same mechanism as a desktop CNC milling machine or router, where the part is built on the fixed surface and the motion in all three coordinates is made by the extruder carriage. Many of the early printers were built in this configuration, but it is very rarely used in modern practice.	2d

As with most mechatronic and coordinate-based manufacturing systems [16-20], the mechanical compliance and vibration within an FFF machine can induce defects into the produced parts; this can damage or ruin them, or at least, destroy their dimensional accuracy and stability [16, 21-30]. While errors are likely present to some extent in any class of FFF machines, these defects are most common at high speeds and high acceleration rates. The use of higher print speeds is essential for drastically reducing the cost of AM parts and expanding their range of use, but the possible introduction of errors is a concern. The extruder carriage overshoot (Figure 3) is the most damaging in complete, sound parts, as it destroys the shape and dimensions of the part. It also happens to be the one that is the simplest to understand and most related to the extreme position error modeled in the present study. Over-shooting errors are very commonly found errors in FFF machines, and it is visible in the eye. Figure 3 below shows the concept of extruder overshooting. When the extruder carriage is approaching the corner of the part, it is following the calculated path and no defects are occurring (Figure 3a). As it turns the corner (Figure 3b), the extruder carriage overshoots the corner due to system compliance in both the belt and printer frame. The overshoot causes extra tension in the system, resulting in reverse motion, causing the carriage to then undershoot (Figure 3c) as it settles to its correct path. After this cycle is repeated several times, the extruder converges back to its calculated path (Figure 3d) and continues with the construction of the part. A real part with this effect present is shown in Figure 3e, where the white line is the calculated path in the g-code, while the red dashed line is the observed true path taken by the extruder head. It is obvious from the example in Figure 3e that the x-axis overshoot and subsequent settling effectively destroyed the part. Any correction, such as post-process machining, filing, or similar would severely weaken the part and practically guarantee a fracture in the structure under use. The deviation is not minor, as evidenced by the fact that the deviation error is, in a few places, wider than the entire shell thickness of the part.

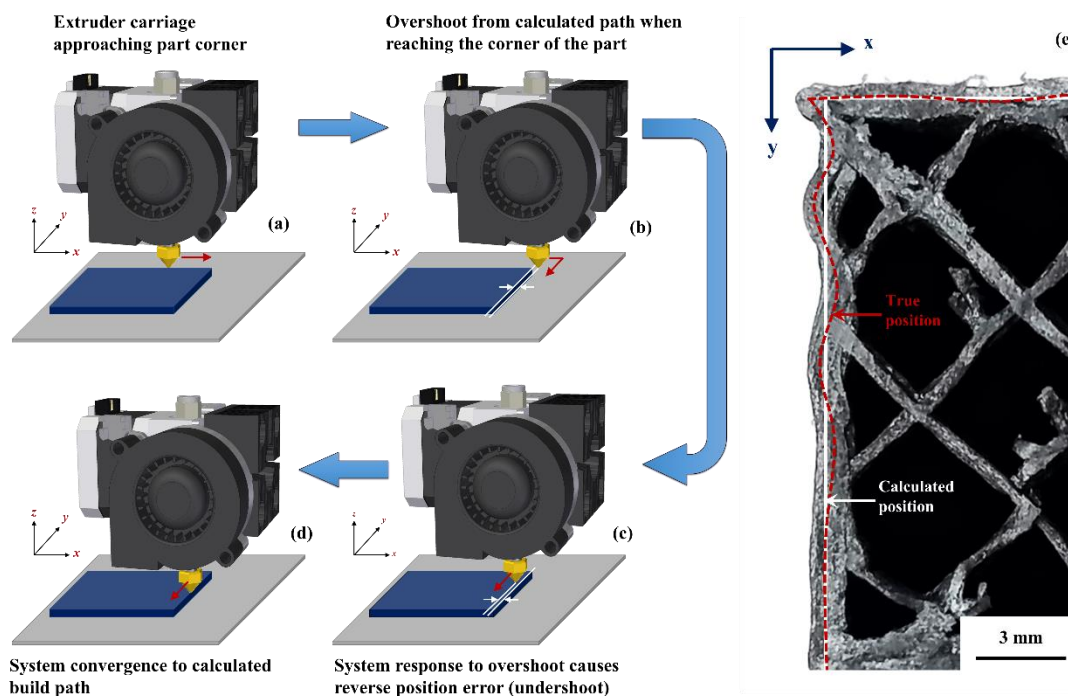


Figure 3: Corner overshoot concept (a-d) and example part (e)

Several sources of the vibration may be identified from studying examples of vibration error; however, the most dominant source by far is certainly the position error of the extruder carriage caused by compliance and vibration in the print frame and the drive belts. Another significant potential source is friction within the system between the moving parts; very small vibrations introduced by friction in the system can be an issue, its effects most likely would not be obvious without a dedicated part inspection. Compared to the magnitude of the mechanical vibration within the system, the vibration from friction will likely be extremely small [31-37]. Therefore, the present study neglects friction vibrations to focus on the error caused in the frame and belts. There is a growing demand in the 3D printing industry for higher print speeds and better accuracy. But as the speed increases, error increases. This research is an attempt to overcome these errors in high speed printing with the available tools and processes and improve them as much as possible. Most effective way of reducing end position errors is implementing control systems. To employ a closed-loop or open-loop control in a system, understanding of the system dynamics is necessary; especially for open-loop controls, a proper dynamic model of the system is required. The main disadvantage of using closed-loop control system is: it limits printing speed, and the state space model is time variant, and states are difficult to measure or predict. With the availability of a dynamic model of the system, predictive control has potential to reduce extreme position error without adding speed limitations by using passive control systems.

The immediate goal of the present study is the derivation and presentation of a well-defined and flexible extruder carriage position model that can be used to drive equations of motion, system state space model, and ultimately be used to design open-loop control systems and optimize the design of the printer frame by introducing passive control elements. Two different techniques are used to find the equations of motion for the conservative carriage motion, the traditional Newton-Euler decomposition method, and the energy-based Lagrange method. The resulting models are compared with each other in detail and should, theoretically, produce the same set of motions equations. Non-linear parameters and damping are added to the motion equations to get a more realistic model of the physical system. A state-space model is developed with the existing equations of motion to present a forward predictive control model. Examples of passive co-designs are presented, and their implementation in state-space are mentioned, which should reduce printing errors. Case study experiments are performed in an existing 3D printer to compare the dynamic model and the ideal input from the motor.

2. Dynamic Model Development

2.1. Extruder Carriage Model Development

The FFF system has three major components: the frame, the extruder carriage, and the build plate. For the purposes of the present study, the motion of the build plate is neglected and assumed to be static relative to the extruder head. The plant for the rest of the printer can be divided into three major systems, each with a compliant connection; these are the (1) frame support structure (desk or workbench), (2) the printer frame, and (3) the extruder motion system. This configuration is valid for all cartesian frame printers. Figure 4 below shows the concept map.

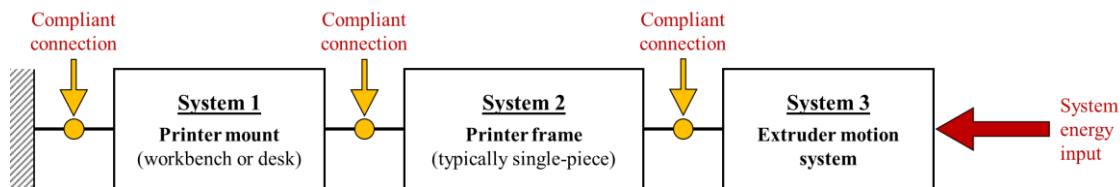


Figure 4: FFF machine plant configuration

The mount is connected to the system ground, while the energy input for the system flows into System 3. The energy for extruder carriage motions comes from motors mounted within the extruder motion system. These motors drive the mechanical components and induce the vibrations into the rest of the system. For all FFF machine types discussed previously, the essential mechanical system is a carriage mounted on a rail and which is driven by a pulley system with at least one motor. After further development of the system model shown in Figure 4, the spring-mass-damper model of the plant used in the extruder carriage motion can be derived (Figure 5) in x-z coordinates. The definitions for each of the variables and parameters are shown in Table 2.

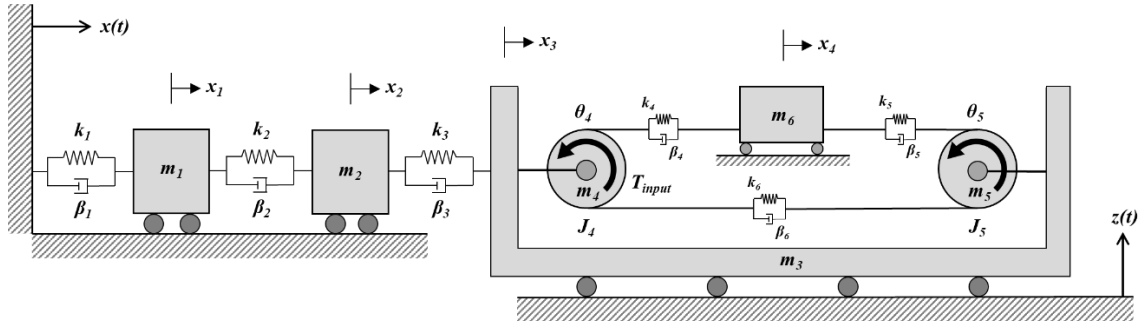


Figure 5: Extruder carriage dynamic model

Table 2: Extruder carriage dynamic model parameters

State Variable		Parameter	
x_1	Position of printer mount (m)	k_1	Stiffness between ground and mount (N/m)
x_2	Position of frame (m)	k_2	Stiffness between mount and frame (N/m)
x_3	Position of extruder motion system (m)	k_3	Stiffness between frame and carriage motion system (N/m)
x_4	Position of extruder carriage (m)	k_4	Stiffness of belt section 1 (N/m)
θ_4	Angular position of Pulley 4 ($radians$)	k_5	Stiffness of belt section 2 (N/m)
θ_5	Angular position of Pulley 5 ($radians$)	k_6	Stiffness of belt section 3 (N/m)
Parameter		β_1	Energy dissipation between ground and mount ($N \cdot s/m$)
m_1	Mass of printer mount (kg)	β_2	Energy dissipation between mount and frame ($N \cdot s/m$)
m_2	Mass of printer frame (kg)	β_3	Energy dissipation between frame and motion ($N \cdot s/m$)
m_3	Mass of extruder motion system frame (kg)	β_4	Energy dissipation in belt section 1 ($N \cdot s/m$)
m_4	Mass of Pulley 4 (kg)	β_5	Energy dissipation in belt section 2 ($N \cdot s/m$)
m_5	Mass of Pulley 5 (kg)	β_6	Energy dissipation in belt section 3 ($N \cdot s/m$)
m_6	Mass of extruder carriage (kg)	$z(t)$	Extruder carriage height (mm)

While the Prusa-frame machines contain the motion of the system in both the x-axis and z-axis, the z-axis velocity is very small. Therefore, it is assumed that the z-axis motion will not directly introduce any detectable vibration into the system and all state variables are in $x(t)$. The specification of the z-height is essential as the stiffness of system components may depend heavily on the height of the extruder carriage.

2.2.1. Conservative Model

This section describes the derivation of the system model previously discussed in terms of Newton-Euler decomposition. This analysis will produce the equations of motion for the conservative system, which does not include any friction or system damping; these will be addressed in a later section. From the perspective of the ground, the motion of the system will reside in three blocks: the machine base, the frame, and the gantry system for the extruder carriage; this is demonstrated in the overall system model shown in Figure 6. The gantry system will have additional motion within it, namely the motion of the drive belt system, but will be a single, self-contained system in the context of the whole system. Below, the system is divided into 2 sub-systems at the point of application of internal force $D(t)$. This system can be modeled as shown in Figure 6 and Figure 7.

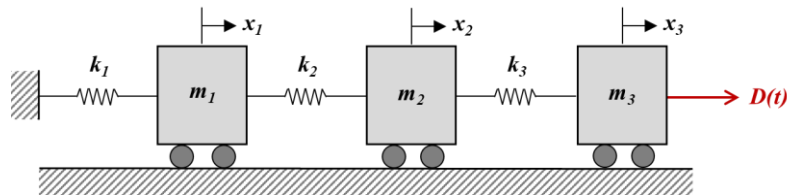


Figure 6: System-level model

Where the force $D(t)$ is the time-variant force introduced into the whole system via the motion of the belt and extruder carriage within the x -axis gantry. This will be modeled in detail later. Mass m_{3t} is defined as the mass of the complete extruder system (Eq 1). The resulting equations of motion for this system are simple to obtain using classic Newtonian laws:

$$m_{3t} = m_3 + m_4 + m_5 + m_6 \quad (1)$$

$$\ddot{x}_1 = -\frac{k_1 + k_2}{m_1}x_1 + \frac{k_2}{m_1}x_2 \quad (2)$$

$$\ddot{x}_2 = \frac{k_2}{m_2}x_1 - \frac{k_2 + k_3}{m_2}x_2 + \frac{k_3}{m_2}x_3 \quad (3)$$

$$\ddot{x}_3 = \frac{k_3}{m_{3t}}x_2 - \frac{k_3}{m_{3t}}x_3 + \frac{D(t)}{m_{3t}} \quad (4)$$

The motion of the extruder carriage is contained within the m_3 block in Figure 4, but any acceleration in this subsystem propagates to the rest of the system. The coupling force $D(t)$ connects the dynamics inside block m_3 to the rest of the system, as described in Figure 7. The input torque is a non-conservative force and will be discussed in a later section.

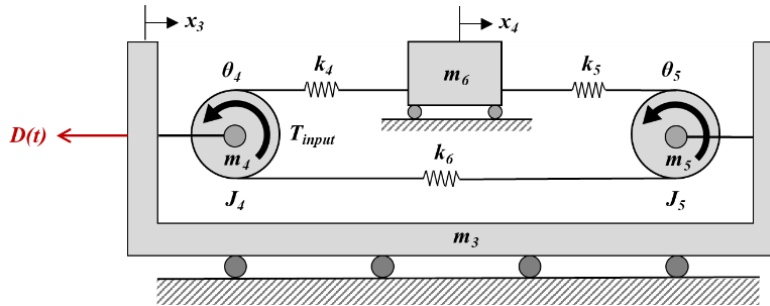


Figure 7: Extruder carriage motion system

While the pulleys are not able to translate within the m_3 block, they are modeled as having both translational and rotational motion from the outside frame. This way, the motion of the whole block can be modeled relative to the motion of the belt and extruder carriage. It is assumed that the belt is a GT2 belt with a relatively low velocity and no significant backlash or slipping in the pulleys [38]. The motion of the extruder system is derived by substituting the value of $D(t)$ as an internal force. Equation of motion of the pulleys and the extruder carriage are derived for the system:

$$\ddot{x}_3 = \frac{k_3}{m_{3t}}x_2 - \frac{(k_3 + k_4 + k_5)}{m_{3t}}x_3 + \frac{(k_4 + k_5)}{m_{3t}}x_4 + \frac{k_4 R}{m_{3t}}\theta_4 + \frac{k_5 R}{m_{3t}}\theta_5 \quad (5)$$

$$\ddot{x}_4 = \frac{(k_4 + k_5)}{m_6}x_3 - \frac{(k_4 + k_5)}{m_6}x_4 - \frac{Rk_4}{m_6}\theta_4 - \frac{Rk_5}{m_6}\theta_5 \quad (6)$$

$$\ddot{\theta}_4 = \frac{2k_4}{m_4 R}x_3 - \frac{2k_4}{m_4 R}x_4 - \frac{2(k_4 + k_6)}{m_4}\theta_4 + \frac{2k_6}{m_4}\theta_5 \quad (7)$$

$$\ddot{\theta}_5 = \frac{2k_5}{m_5 R}x_3 - \frac{2k_5}{m_5 R}x_4 + \frac{2k_6}{m_5}\theta_4 - \frac{2(k_5 + k_6)}{m_5}\theta_5 \quad (8)$$

Using the same notation and assumptions as the Newton-Euler model previously described, the equations of motion are derived in terms of the system energy using the Lagrange method. This method gives the user some additional insight into the energy-transfer aspects of the system that a force-based method like Newton-Euler is not able to provide [39]. It is also the check for the correctness of the Newton-Euler model, as the methods should independently provide the same equations of motion for a physically conservative system. The Lagrangian of the system is described by:

$$L = T - V \quad (9)$$

where V describes the potential energy in the system and T describes the kinetic energy. In this problem, each of the energy types has six equations, since there are six state variables. The equations of motion for the system are given by,

$$\frac{d}{dt} \left(\frac{\partial L}{\partial \dot{q}} \right) - \frac{\partial L}{\partial q} = 0 \quad (10)$$

considering only the conservative terms and neglecting friction and damping in the system. On deriving the equation of motion using Lagrange, it is found that the final equations of motion in Newton-Euler conservative model (Eqs 1-8) are exactly the same as the equations of motion in Lagrange model. Both these models have been derived independently and verify the correctness of the model and its equations of motion.

Note that this model assumes that the belt stiffness is constant throughout the motion of the extruder carriage. The stiffness is not constant in practice, but a function of a characteristic stiffness and the belt length; belt stiffness will be examined in a later section. This model of the system allows the input of angular acceleration into one of the pulleys which then transmits to the complete system. It provides a way for tracking motion in all of the three system blocks shown in Figure 4. The derived model is not a linear model, as some of the parameters may be highly non-linear, which should be established. The overall goal of this model is to track x_4 relative to an ideal trajectory, in order to find the carriage position error. The effects of non-conservative system forces, particularly those from damping and friction, will be discussed later.

2.2.2. Non-Conservative Model

Figure 8 shows the full system under consideration, including both conservative and non-conservative forces. The system is shown here in a decomposed state in order to use the Newton-Euler method for deriving the full model, including the stiffnesses, the dampers, and the input torque. The equations are derived similar to Newton Euler Conservative model shown earlier.

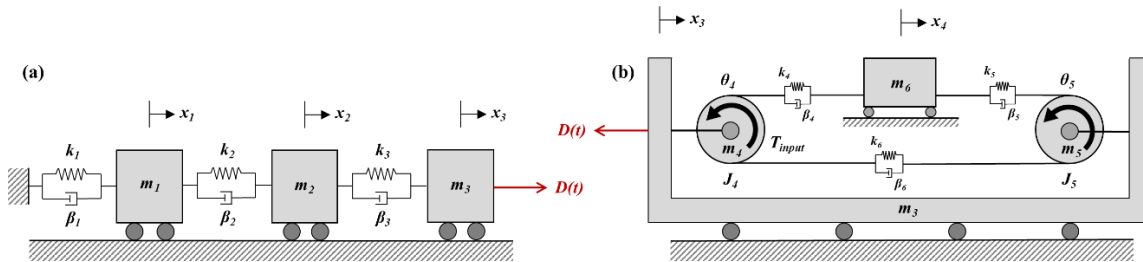


Figure 8: Extruder carriage system considering both conservative and non-conservative forces

The non-conservative equations of motion are:

$$\ddot{x}_1 = -\frac{k_1 + k_2}{m_1} x_1 + \frac{k_2}{m_1} x_2 - \frac{\beta_1 + \beta_2}{m_1} \dot{x}_1 + \frac{\beta_2}{m_1} \dot{x}_2 \quad (9)$$

$$\ddot{x}_2 = \frac{k_2}{m_2} x_1 - \frac{k_2 + k_3}{m_2} x_2 + \frac{k_3}{m_2} x_3 + \frac{\beta_2}{m_2} \dot{x}_1 - \frac{\beta_2 + \beta_3}{m_2} \dot{x}_2 + \frac{\beta_3}{m_2} \dot{x}_3 \quad (10)$$

$$\ddot{x}_3 = \frac{k_3}{m_{3t}}x_2 - \frac{(k_3 + k_4 + k_5)}{m_{3t}}x_3 + \frac{(k_4 + k_5)}{m_{3t}}x_4 + \frac{k_4R}{m_{3t}}\theta_4 + \frac{k_5R}{m_{3t}}\theta_5 + \frac{\beta_3}{m_{3t}}\dot{x}_2 - \frac{(\beta_3 + \beta_4 + \beta_5)}{m_{3t}}\dot{x}_3 + \frac{(\beta_4 + \beta_5)}{m_{3t}}\dot{x}_4 + \frac{\beta_4R}{m_{3t}}\dot{\theta}_4 + \frac{\beta_5R}{m_{3t}}\dot{\theta}_5 \quad (11)$$

$$\ddot{x}_4 = \frac{(k_4 + k_5)}{m_6}x_3 - \frac{(k_4 + k_5)}{m_6}x_4 - \frac{Rk_5}{m_6}\theta_5 - \frac{Rk_4}{m_6}\theta_4 + \frac{(\beta_4 + \beta_5)}{m_6}\dot{x}_3 - \frac{\beta_4 + \beta_5}{m_6}\dot{x}_4 - \frac{\beta_4R}{m_6}\dot{\theta}_4 - \frac{\beta_5R}{m_6}\dot{\theta}_5 \quad (12)$$

$$\ddot{\theta}_4 = -\frac{2k_4}{m_4R}x_4 + \frac{2k_4}{m_4R}x_3 + \frac{2(k_4 + k_6)}{m_4}\theta_4 + \frac{2k_6}{m_4}\theta_5 + \frac{2\beta_4}{m_4R}\dot{x}_3 - \frac{2\beta_4}{m_4R}\dot{x}_4 - \frac{2(\beta_4 + \beta_6)}{m_4}\dot{\theta}_4 + \frac{2\beta_6}{m_4}\dot{\theta}_5 + \frac{2T_{input}}{m_4R^2} \quad (13)$$

$$\ddot{\theta}_5 = \frac{2k_5}{m_5R}x_3 - \frac{2k_5}{m_5R}x_4 - \frac{2(k_5 + k_6)}{m_5}\theta_5 + \frac{2k_6}{m_5}\theta_4 + \frac{2\beta_5}{m_5R}\dot{x}_3 - \frac{2\beta_5}{m_5R}\dot{x}_4 + \frac{2\beta_6}{m_5}\dot{\theta}_4 - \frac{2(\beta_5 + \beta_6)}{m_5}\dot{\theta}_5 \quad (14)$$

2.2. Additional Model Considerations

The system contains non-conservative forces along with linear and non-linear parameters. The major non-conservative forces in such a system consist of friction, damping, and the applied torque into the system to drive it. Several of the stiffnesses in the system, while conservative, are non-linear. For the current problem, these are the stiffnesses of the frame-gantry interface and the stiffnesses of the drive belts. All these aspects of the system must be accounted for.

2.2.1. System Friction

The extruder carriage system of a typical printer is supported by hard rubber wheels sitting on a square aluminum rail or by a lubricated linear bearing. Commonly, the extruder carriage system is supported by a series of linear ball bearings which typically have a friction coefficient less than $\mu = 0.005$ [40] when properly maintained. The main source friction present in this system is the rolling resistance friction between the extruder carriage and the extruder frame rail, which is much smaller compared to sliding friction. Typical rolling resistance coefficient for such a system varies from $\mu = 0.002 - 0.005$. The normal force on the joint comes exclusively from the mass of the extruder carriage, which is heavily restricted by the size and strength of the printer frame. For nearly all cases, the weight of the extruder carriage is less than $F_n = 10 \text{ N}$ in normal atmospheric conditions (i.e. the mass of the extruder carriage, its components, and its support structure are typically less than 1 kg in mass). Therefore, it is reasonable for this problem to neglect the effects of friction between the extruder carriage and its rails. There are no other significant sources of friction in the system.

2.2.2. System Damping

With the assumption of negligible friction, the remaining non-conservative forces are from the dampers in the system. The dampers are all natural and come from the printer mount, the frame, and the belts driving the extruder carriage, as shown in Figure 6. Both the methods previously described can accommodate non-conservative forces into the equations of motion. However, since the Newton-Euler method is based on forces in the system and not energy, the analysis with non-conservative forces is more easily and intuitively done using the Newton-Euler method. For the belts in this model, the dampers are assumed to be lumped linear dampers with constant coefficients. An extensive study by Shangguan & Zeng [41] found that the damping coefficient in drive belts was dependent on the excitation frequency, but not on the belt length. Significant modeling and experimental work under various conditions showed this to be the case, validating the assumption of constant coefficients for the belts. The other three dampers in the system,

those of the workbench (β_1), the frame (β_2), and the interface between the frame and the extruder carriage (β_3) are also assumed linear with constant coefficients. This assumption for β_1 and β_2 are justified due to the static and non-changing natural state of these structures. For most FFF machines, this interface consists of a linear bearing riding on a linear rail of some kind, or wheels mounted on a rectangular aluminum rail. This is a single-degree-of-freedom problem, so it logically has a constant damping coefficient for a specified beam length. The structural damping work by Hunt *et al.* [42], Liu [43], and Perez-Pena *et al.* [44] support this assumption as well.

2.2.3. System Stiffness

The stiffnesses in this model are a mixture of both linear and non-linear springs, each of which depend on the specific FFF printer configuration under study. The simplest to analyze are the printer base and frame stiffnesses, which are clearly linear, as they are static structures and do not significantly change shape during the process. Therefore,

$$k_1, k_2 \rightarrow \text{constant} \quad (15)$$

The stiffness of the interface between the frame and the extruder gantry (k_3) is heavily dependent on the exact configuration of the plant, as well as the position of the connector on the rail. It may be linear or non-linear, depending on the exact configuration used; for the application to a specific machine configuration, this relationship must be established. All that is known for the general model is that it will be a function of Z . Therefore,

$$k_3 \rightarrow f(Z) \quad (16)$$

The belt section stiffnesses are the most complex to model, as the top two (k_4 and k_5) change length continuously during the processing. The standard model for the stiffness of belts [45] that are changing length with time is:

$$k = C_{sp} \frac{b}{L(t)} \quad (17)$$

where C_{sp} is the characteristic stiffness of the belt, b is the belt width, and $L(t)$ is the length at time t . This assumes that the belts do not experience significant stretching during use. The results of the belt stiffness study [45] show that no significant stretching occurs. Therefore, the stiffness of the belt is highly non-linear and depends solely on the states:

$$k_4 = C_{sp} \frac{b}{\delta_4} = C_{sp} \frac{b}{L_1 + x_4} \quad (18)$$

$$k_5 = C_{sp} \frac{b}{\delta_5} = C_{sp} \frac{b}{L_2 - x_4} \quad (19)$$

$$k_6 = C_{sp} \frac{b}{\delta_6} = \frac{C_{sp} b}{L} \rightarrow \text{constant} \quad (20)$$

This assumes that characteristic stiffness C_{sp} and belt width b are known and the same values (linear or non-linear) for both belt sections. L_1 is the length of belt from left side pulley to the extruder, L_2 is the length of belt from extruder to the right-side pulley and L is the distance between centers of the driver and driven pulleys. The value of C_{sp} can be reasonably approximated as a constant value for the GT2 belts [45] used on most FFF machines. The value of the final stiffness k_6 is assumed to be constant since the length of the belt does not change during processing and the width of the belt is constant.

2.2.4. Extruder Carriage Belt Pre-Load

The effect of belt pre-load is certainly a consideration for any belt-driven system [41], as it influences the initial value of belt stiffness. The typical belt pre-load for FFF machines varies from 35 N – 45 N , enough to keep

the belt section from slacking under acceleration but not enough to significantly stretch the belt. As shown by Wang *et al.* [45] the set of GT2 belt had an average failure tension of about 615 N, so a pre-load of 35 N – 45 N, will not significantly affect deflection. As previously described, the effect of the pre-load is to set the initial belt stiffness; it is assumed that the belt had time to settle after being pre-loaded before being used, so the value of the pre-load is constant in all belt sections. Therefore,

$$k_4 = C_{sp} \frac{b}{L_1 + x_4} + \frac{F_{pl}}{L_0} \quad (21)$$

$$k_5 = C_{sp} \frac{b}{L_2 - x_4} + \frac{F_{pl}}{L_0} \quad (22)$$

$$k_6 = \frac{C_{sp}b}{L} + \frac{F_{pl}}{L_0} \rightarrow \text{constant} \quad (23)$$

The value of F_{pl}/L_0 is constant and calculated before the start of the extruder carriage motion. The value of L_0 is approximated to be the length of the belt.

2.3. State Space Equations

Considering the friction, damping, and belt stiffness changes, as well as the torque input, in the system during processing, a non-linear state space model was developed with the states:

$$[z_1 \ z_2 \ z_3 \ z_4 \ z_5 \ z_6 \ z_7 \ z_8 \ z_9 \ z_{10} \ z_{11} \ z_{12}] = [x_1 \ \dot{x}_1 \ x_2 \ \dot{x}_2 \ x_3 \ \dot{x}_3 \ x_4 \ \dot{x}_4 \ \theta_4 \ \dot{\theta}_4 \ \theta_5 \ \dot{\theta}_5] \quad (23)$$

Using Eq. 23 and Eqs. 9-14, the state derivatives can be calculated as:

$$\dot{z}_1 = \dot{x}_1 = z_2 \quad (24)$$

$$\dot{z}_2 = \ddot{x}_1 = -\frac{k_1 + k_2}{m_1} z_1 + \frac{k_2}{m_1} z_3 - \frac{\beta_1 + \beta_2}{m_1} z_2 + \frac{\beta_2}{m_1} z_4 \quad (25)$$

$$\dot{z}_3 = \dot{x}_2 = z_4 \quad (26)$$

$$\dot{z}_4 = \ddot{x}_2 = \frac{k_2}{m_2} z_1 - \frac{k_2 + k_3}{m_2} z_3 + \frac{k_3}{m_2} z_5 + \frac{\beta_2}{m_2} z_2 - \frac{\beta_2 + \beta_3}{m_2} z_4 + \frac{\beta_3}{m_2} z_6 \quad (27)$$

$$\dot{z}_5 = \dot{x}_3 = z_6 \quad (28)$$

$$\begin{aligned} \dot{z}_6 = \ddot{x}_3 = & \frac{k_3}{m_{3t}} z_3 - \frac{(k_3 + k_4 + k_5)}{m_{3t}} z_5 + \frac{(k_4 + k_5)}{m_{3t}} z_7 + \frac{k_4 R}{m_{3t}} z_9 + \frac{k_5 R}{m_{3t}} z_{11} \\ & + \frac{\beta_3}{m_{3t}} z_4 - \frac{(\beta_3 + \beta_4 + \beta_5)}{m_{3t}} z_6 + \frac{(\beta_4 + \beta_5)}{m_{3t}} z_8 + \frac{\beta_4 R}{m_{3t}} z_{10} + \frac{\beta_5 R}{m_{3t}} z_{12} \end{aligned} \quad (29)$$

$$\dot{z}_7 = \dot{x}_4 = z_8 \quad (30)$$

$$\begin{aligned} \dot{z}_8 = \ddot{x}_4 = & \frac{(k_4 + k_5)}{m_6} z_5 - \frac{(k_4 + k_5)}{m_6} z_7 - \frac{Rk_5}{m_6} z_{11} - \frac{Rk_4}{m_6} z_9 + \frac{(\beta_4 + \beta_5)}{m_6} z_6 \\ & - \frac{\beta_4 + \beta_5}{m_6} z_8 - \frac{\beta_4 R}{m_6} z_{10} - \frac{\beta_5 R}{m_6} z_{12} \end{aligned} \quad (31)$$

$$\dot{z}_9 = \dot{\theta}_4 = z_{10} \quad (32)$$

$$\dot{z}_{10} = \ddot{\theta}_4 = -\frac{2k_4}{m_4 R} z_7 + \frac{2k_4}{m_4 R} z_5 - \frac{2(k_4 + k_6)}{m_4} z_9 + \frac{2k_6}{m_4} z_{11} + \frac{2\beta_4}{m_4 R} z_6 - \frac{2\beta_4}{m_4 R} z_8 - \frac{2(\beta_4 + \beta_6)}{m_4} z_{10} + \frac{2\beta_6}{m_4} z_{12} + \frac{2T_{input}}{m_4 R^2} \quad (33)$$

$$\dot{z}_{11} = \dot{\theta}_5 = z_{12} \quad (34)$$

$$\dot{z}_{12} = \ddot{\theta}_5 = \frac{2k_5}{m_5 R} z_5 - \frac{2k_5}{m_5 R} z_7 - \frac{2(k_5 + k_6)}{m_5} z_{11} + \frac{2k_6}{m_5} z_9 + \frac{2\beta_5}{m_5 R} z_6 - \frac{2\beta_5}{m_5 R} z_8 + \frac{2\beta_6}{m_5} z_{10} - \frac{2(\beta_5 + \beta_6)}{m_5} z_{12} \quad (35)$$

The state-space equations of a system are of the form:

$$\dot{X} = AX + Bu \quad (36)$$

$$Y = CX + Du \quad (37)$$

In the present study $D=0$ for Eq 37 and matrix C depends on the variable to observe, which in this study can be taken as the extruder carriage position and velocity. Therefore,

$$[C] = [0 \ 0 \ 0 \ 0 \ 0 \ 0 \ 1 \ 1 \ 0 \ 0 \ 0 \ 0]^T \quad (38)$$

$$[A] = \quad (39)$$

$$\begin{bmatrix}
 0 & 1 & 0 & 0 & 0 & 0 & 0 & 0 & 0 & 0 & 0 & 0 \\
 \frac{k_1 + k_2}{m_1} & -\frac{\beta_1 + \beta_2}{m_1} & \frac{k_2}{m_1} & \frac{\beta_2}{m_1} & 0 & 0 & 0 & 0 & 0 & 0 & 0 & 0 \\
 0 & 0 & 0 & 1 & 0 & 0 & 0 & 0 & 0 & 0 & 0 & 0 \\
 \frac{k_2}{m_2} & \frac{\beta_2}{m_2} & -\frac{k_2 + k_3}{m_2} & -\frac{\beta_2 + \beta_3}{m_2} & \frac{k_3}{m_2} & \frac{\beta_3}{m_2} & 0 & 0 & 0 & 0 & 0 & 0 \\
 0 & 0 & 0 & 0 & 0 & 1 & 0 & 0 & 0 & 0 & 0 & 0 \\
 0 & 0 & \frac{k_3}{m_{3t}} & \frac{\beta_3}{m_{3t}} & -\frac{(k_3 + k_4 + k_5)}{m_{3t}} & -\frac{(\beta_3 + \beta_4 + \beta_5)}{m_{3t}} & \frac{(k_4 + k_5)}{m_{3t}} & \frac{(\beta_4 + \beta_5)}{m_{3t}} & \frac{k_4 R}{m_{3t}} & \frac{\beta_4 R}{m_{3t}} & \frac{k_5 R}{m_{3t}} & \frac{\beta_5 R}{m_{3t}} \\
 0 & 0 & 0 & 0 & 0 & 0 & 0 & 1 & 0 & 0 & 0 & 0 \\
 0 & 0 & 0 & 0 & \frac{(k_4 + k_5)}{m_6} & \frac{(\beta_4 + \beta_5)}{m_6} & -\frac{(k_4 + k_5)}{m_6} & -\frac{\beta_4 + \beta_5}{m_6} & -\frac{Rk_4}{m_6} & -\frac{\beta_4 R}{m_6} & -\frac{Rk_5}{m_6} & -\frac{\beta_5 R}{m_6} \\
 0 & 0 & 0 & 0 & 0 & 0 & 0 & 0 & 0 & 1 & 0 & 0 \\
 0 & 0 & 0 & 0 & \frac{2k_4}{m_4 R} & \frac{2\beta_4}{m_4 R} & -\frac{2k_4}{m_4 R} & -\frac{2\beta_4}{m_4 R} & -\frac{2(k_4 + k_6)}{m_4} & -\frac{2(\beta_4 + \beta_6)}{m_4} & \frac{2k_6}{m_4} & \frac{2\beta_6}{m_4} \\
 0 & 0 & 0 & 0 & 0 & 0 & 0 & 0 & 0 & 0 & 0 & 1 \\
 0 & 0 & 0 & 0 & \frac{2k_5}{m_5 R} & \frac{2\beta_5}{m_5 R} & -\frac{2k_5}{m_5 R} & -\frac{2\beta_5}{m_5 R} & \frac{2k_6}{m_5} & \frac{2\beta_6}{m_5} & -\frac{2(k_5 + k_6)}{m_5} & -\frac{2(\beta_5 + \beta_6)}{m_5}
 \end{bmatrix}$$

$$[B] = \left[0 \ 0 \ 0 \ 0 \ 0 \ 0 \ 0 \ 0 \ 0 \ 0 \ \frac{2}{m_4 R^2} \ 0 \ 0 \right]^T \quad (40)$$

$$[X] = [z_1 \ z_2 \ z_3 \ z_4 \ z_5 \ z_6 \ z_7 \ z_8 \ z_9 \ z_{10} \ z_{11} \ z_{12}]^T \quad (41)$$

$$u = T_{input} \quad (42)$$

2.4. Ideal Extruder Motion

The theoretical path taken by the extruder carriage can be calculated, knowing that the torque on the pulley can be translated directly into linear motion. The assumption is made that there is no compliance or vibration in the belt, and the frame and support are perfectly rigid. The motor will provide torque to rotate the pulleys and extruder at same acceleration ideally. This is the “ideal” motion that is applied by the motor to the pulley, which should be calculated in order to compare this ideal to the system behavior.

$$T_{input}(t) = m_6\ddot{x}_4R + \frac{J_4\ddot{x}_4}{R} + \frac{J_5\ddot{x}_4}{R} \quad (43)$$

$$\ddot{x}_4 = \frac{T_{input}(t)}{m_6R + 0.5m_4R + 0.5m_5R} \quad (44)$$

2.5. System Input Torque

In the model presented in this study, the torque of the input motor drives the dynamics of the system via Pulley 4, the driver pulley. The inputs to the stepper motor which control the torque and rotation speed are the input voltage, the input current, and the impedance of the motor. Most FFF systems use either 12V or 24V power supplies, depending on the setup of the machine, and have a constant resistance. The torque input is a function of time and depending on the part to be printed and the print settings decided, the torque will consist of a ramp-up and a steady state torque. It is assumed in this model that the motor voltage and torque are controlled externally to the system and that they are load-independent as long as the load does not exceed the rated torque for the motor [46-49]. In a well-adjusted and correctly functioning FFF system, the moving parts of the machine do not directly contact the part being made except along a small bead of molten plastic [50-51]. Unlike in a subtractive manufacturing process, there is very little mechanical resistance in the system motion, so it is predicted that the stepper motor torque will not exceed its maximum rating under any normal working conditions. Even in practice, the holding torque of the stepper motor will never be reached, as that amount of torque is not generally required to run the printer except at very high speed print and even then, the holding torque is rarely reached.

$$\tau_{applied} < \tau_{holding} \quad (45)$$

The stepper motor delivers the required motion using pulses of current. The actual input to the stepper motor does not contain specific information about the amount of torque to be delivered. Depending on the frequency of pulses and the length of pulse, the extruder accelerates, decelerates or moves at constant velocity. These parameters are converted to G codes and then fed to the printer in the form of pulse frequency and duration. There are 3 major factors affecting the extruder motion profile in a print: acceleration, velocity and jerk. Figure 9 shows a general velocity profile for 1 cycle of an input waveform in a printer and Table 3 describes the respective activities occurring at different time periods chronically during 1 cycle. Table 4 shows the major parameters set on the printer to achieve the input waveform shown in Figure 9.

In 3D printers, jerk is defined as the velocity before or after the extruder follows the defined acceleration during ramp-down and ramp-up respectively. In simpler terms, the extruder moves at maximum acceleration until it reaches the jerk velocity, after which the extruder follows the defined acceleration profile. In the same way when the extruder is slowing down, it will move at maximum deceleration to 0 once the extruder reaches the jerk velocity. In the printer being studied, this maximum acceleration is set to 1000 mm/s² defined in the printer. Jerk and acceleration parameters are chosen such that there is a balance between the quality of print and time required for printing.

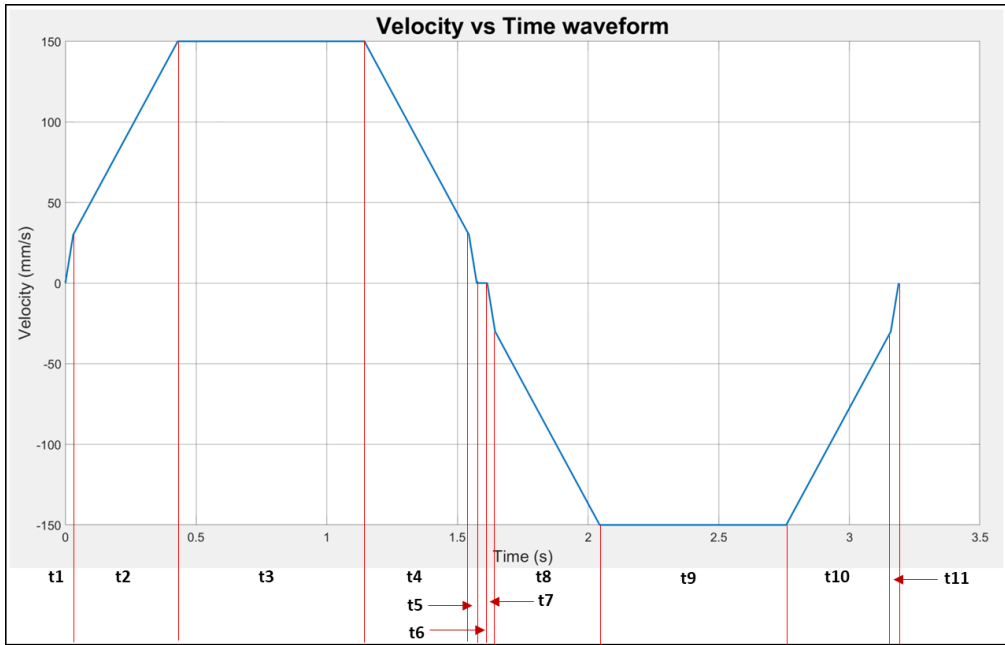


Figure 9: Velocity vs time profile of a typical printer input waveform

Table 3: Activities in various time periods for 1 cycle in an input waveform

Time Period	Activity
0-t1	Maximum acceleration up to jerk velocity
t2	Constant acceleration up to desired velocity
t3	Constant velocity
t4	Constant deacceleration up to jerk velocity
t5	Maximum deacceleration up to 0 velocity
t6	Z-hop time: Time for extruder to hop to next layer
t7	Maximum deacceleration up to negative jerk velocity
t8	Constant deacceleration up to negative desired velocity
t9	Constant velocity (negative)
t10	Constant acceleration up to negative jerk velocity
t11	Maximum acceleration up to 0 velocity

Table 4: Print parameters to obtain the input waveform in Figure 9

Parameters	Value	Units
Maximum acceleration	1000	mm/s ²
Print acceleration	300	mm/s ²
Print velocity	150	mm/s
Jerk	30	mm/s
Print distance (1 direction)	180	mm
Z-hop time	0.04	s

3. Case Study Experiments

Case experiments were performed on a Voxelab Aquila S2 3D Printer (Figure 10). The X-axis, Y-axis and Z-axis movement of the printer is controlled by 3 rotational stepper motors. The X-axis carriage is connected to the motor using a GT2 timing belt. The z-axis movement is controlled by a lead screw connected to the extruder assembly and the motor. The print bed offers y-axis movement similar to X-axis by using a timing belt. The printer offers a maximum acceleration of 1000 mm/s^2 and a maximum velocity of 200 mm/s in X and Y directions.

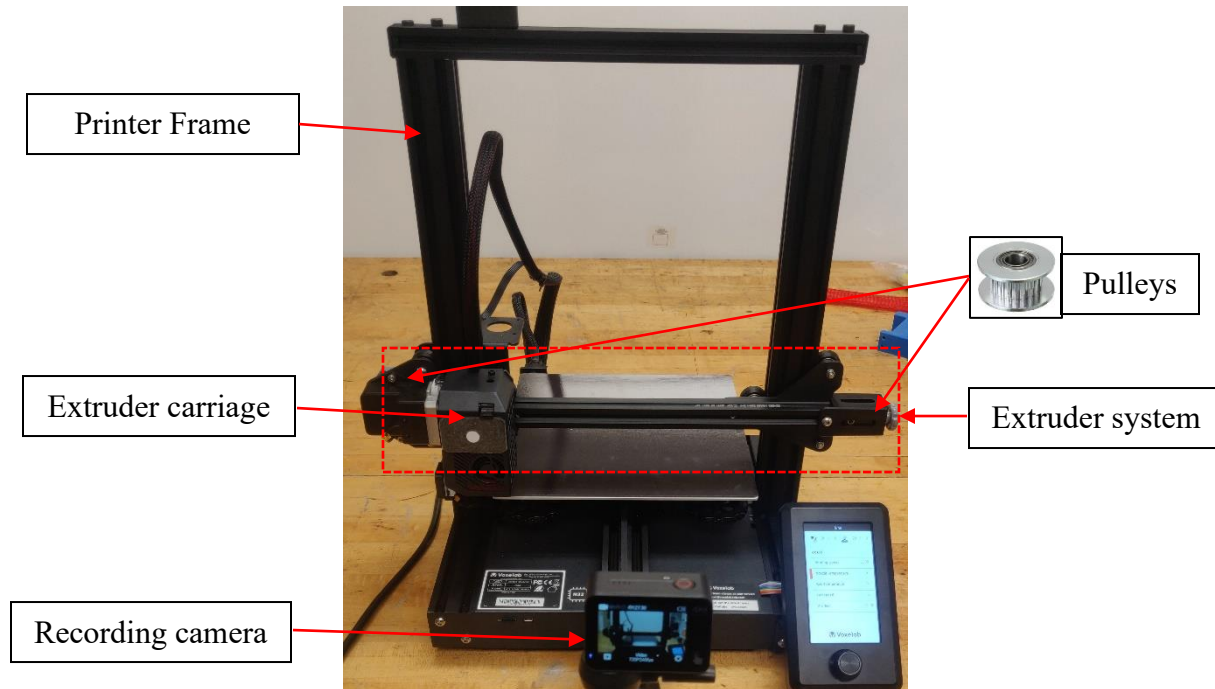


Figure 10: Voxelab Aquila S2 3D printer used for experiments

3.1. Design of Experiments

To understand the printer under different parameter conditions, case studies were performed by varying the major printing parameters: print speed and print acceleration. The z-height was varied to measure the printer performance for different layers when printing. The z-height is also taken as a major parameter in this study as the stiffness varies with height, affecting the extruder carriage motion. The values for speed and acceleration used for this study are typically used for balanced time and quality print and for faster prints. 4 values each of speed, acceleration and height were used to perform the case studies. Orthogonal array method was used for the design of experiments to get better results on comparatively lower samples. Using orthogonal arrays, 16 cases were formed as shown in Table 5, with their parameters.

A simple 3D model of a rectangular block of 180 mm length, 1 layer thick (0.4mm) and 5mm tall was developed in SOLIDWORKS 2021 modelling software. The model was then sliced using Ultimaker Cura 5.2.1 (slicing software) which produced a mesh ready to be printed. The desired parameters of speed, acceleration, jerk and height settings were fed into the slicing software to produce the desired sliced G-codes. These G-codes were then fed into the printer.

Table 5: Parameters for experimental case studies

Test	Size (mm)	Max Speed Limit (mm/s)	Acceleration (mm/s ²)	Height (mm)	Jerk (mm/s)
1	180 × 5 × 0.4	150	200	0-1	10
2	180 × 5 × 0.4	150	300	50-51	10
3	180 × 5 × 0.4	150	400	100-101	10
4	180 × 5 × 0.4	150	500	150-151	10
5	180 × 5 × 0.4	250	200	50-51	10
6	180 × 5 × 0.4	250	300	0-1	10
7	180 × 5 × 0.4	250	400	150-151	10
8	180 × 5 × 0.4	250	500	100-101	10
9	180 × 5 × 0.4	350	200	100-101	10
10	180 × 5 × 0.4	350	300	150-151	10
11	180 × 5 × 0.4	350	400	0-1	10
12	180 × 5 × 0.4	350	500	50-51	10
13	180 × 5 × 0.4	500	200	150-151	10
14	180 × 5 × 0.4	500	300	100-101	10
15	180 × 5 × 0.4	500	400	50-51	10
16	180 × 5 × 0.4	500	500	0-1	10
R1	180 × 5 × 0.4	50	25	0-1	-
R2	180 × 5 × 0.4	50	25	50-51	-
R3	180 × 5 × 0.4	50	25	100-101	-
R4	180 × 5 × 0.4	50	25	150-151	-

3.2. Extruder Carriage Tracking

The printer was set on a very heavy wooden table such that the vibration effect on the table can be assumed as grounded. Figure 11 shows the experimental setup with the printer and camera. The printer head movement was recorded by using a 240 fps CamPark X30 camera. Each frame of the video was converted to gray scale in MATLAB and then cropped and edited to track the extruder carriage movement. Pixel brightness data and shape recognition were used to filter out the noise from the video. To ease grayscale tracking, a white sticker of 10 mm diameter was attached to the black extruder carriage as can be seen in Figure 10. The video files for the entire run were too large for MATLAB, and so the videos were cropped to view 2 cycles for each case. MATLAB vision was able to track the extruder carriage for all the frames in the video; one of the recorded tracking frames is shown in Figure 12. The original extruder frame can be seen above, and the tracking frame can be seen below in Figure 12. The white line in Figure 12 below is the position of the extruder sticker as it moves in the frame.



Figure 11: Experimental setup to record extruder carriage movement

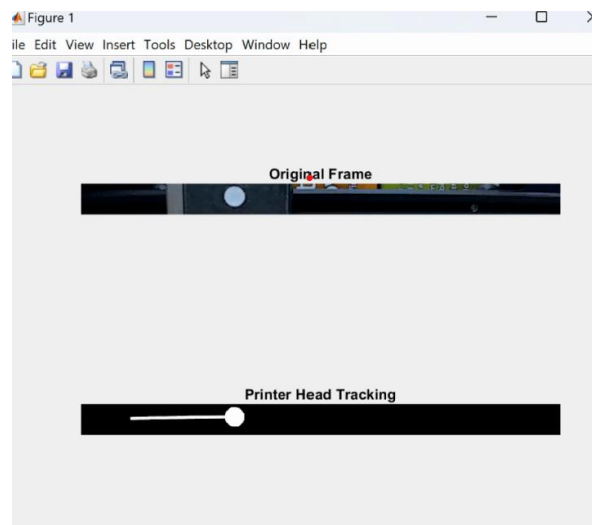


Figure 12: Tracking of extruder carriage using MATLAB vision

The tracking data is initially stored in pixels which are then converted to distance. To reference the extruder position and get more accurate data with minimum error, reference runs were recorded and analyzed. The last 4 entries in Table 5 from test no. R1 to R4 show the reference runs for different z-heights. These reference tests were set extremely slowly such that it can be assumed the extruder had negligible position error during these tests. The end-to-end pixel data of these reference runs were used to set the position reference for each z-height test, which was later used to calculate the extruder position for the tests.

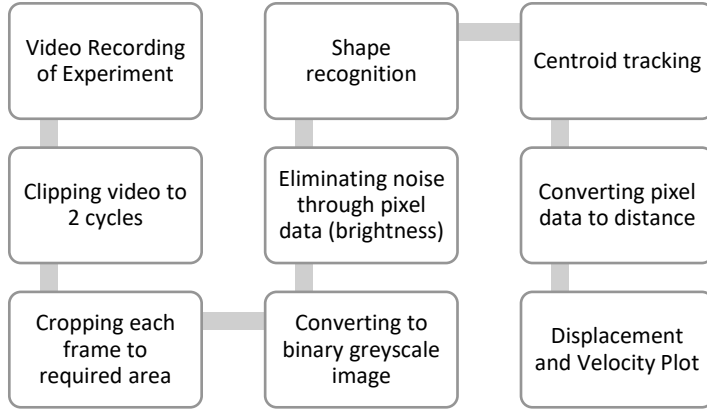


Figure 13: Stepwise flowchart for extruder carriage tracking

3.3. Printer Properties

To get a better understanding and a realistic representation of the printer studied, physical properties of the printer must be studied. Physical parameters of the printer like mass, and stiffness and damping of belt and printer frame were experimentally measured and calculated using FEA Ansys modelling to provide a closer comparison between the dynamic model and the experimental results. Mass of each of the components relevant to this research were measured using a weight scale. Belt stiffness was measured through stress-strain test using a universal testing machine. Using the belt stiffness, belt constant C_{sp} was measured using Eq. 46.

$$C_{sp} = \frac{EtL_i}{L} \quad (46)$$

Where E is the belt stiffness, t is belt thickness, L_i is the elongated belt length, and L is the normal belt length. Belt damping was also measured using a universal testing machine by gradually loading and unloading the belt. The stress strain values were recorded to form a hysteresis curve. Damping ratio was calculated from the hysteresis curve by using Eq 47.

Table 6: Printer parameters

Parameters	Value	Units	Parameters	Value	Units
m_2	6.201	kg	k_2	5000	N/m
m_3	0.721	kg	k_3 at 0mm	7.99×10^9	N/m
m_4	0.17	kg	k_3 at 50mm	1.28×10^{10}	N/m
m_5	0.17	kg	k_3 at 100mm	1.88×10^{10}	N/m
m_6	0.611	kg	k_3 at 150mm	2.12×10^{10}	N/m
R	8	mm	C_{sp}	1.74×10^6	N/m
F_{pt}	44.74	N	L	350	mm
L_1	80	mm	L_0	750.265	mm
b	6	mm	β_4	118.725	Ns/m
β_2	1450	Ns/m	β_5	118.725	Ns/m
β_3	850	Ns/m	β_6	118.725	Ns/m

$$D = \frac{E_h}{4\pi E_e} \quad (47)$$

Where D is damping ratio, E_h is the area under hysteresis loop, and E_e is the triangle area enclosed by maximum stress and strain measured. The damping coefficient from damping ratio was calculated using Eq 48.

$$\beta = 2D\sqrt{km} \quad (48)$$

Where β is the damping coefficient, k is the belt stiffness and m is the belt mass. A printer frame model was designed in SOLIDWORKS to perform FEA analysis in ANSYS to calculate the stiffness of the printer frame at the four heights. Table 6 presents the printer parameters obtained. Note that in the experimental setup there is no mount between the printer and ground and hence no stiffness and damping between ground and m_1 .

3.4. Model Analysis

The dynamic model of the system follows closely with the ideal model. Figure 14 shows the displacement plot for ideal and dynamic model for Test 3 parameters from Table 5. The rectangular dotted box zooms the peak displacement region and expands below to show that the error between the two models is small and slight increase when there is a change of direction. Figure 15 presents the corresponding velocity vs time plot for the same parameters. The dynamic model velocity follows closely with the ideal velocity and the error occurs at transitions and peak velocity regions as expected. The experimental results for displacement and velocity for Test 3 are shown in Figure 16. The velocity signal has noises due to vision tracking and partly vibration, and is denoised in MATLAB using 'loess' method. The peak displacement is marked in the plot, occurring at the change of direction region. This error is an extruder overshooting error that affects the dimension of the printed part. The displacement plot is very similar to the dynamic and ideal model plot. Although the velocity plot is harder to compare, if observed closely, the velocity plot has similar transitional trends with the ideal and dynamic model velocity plot with similar peak velocities.

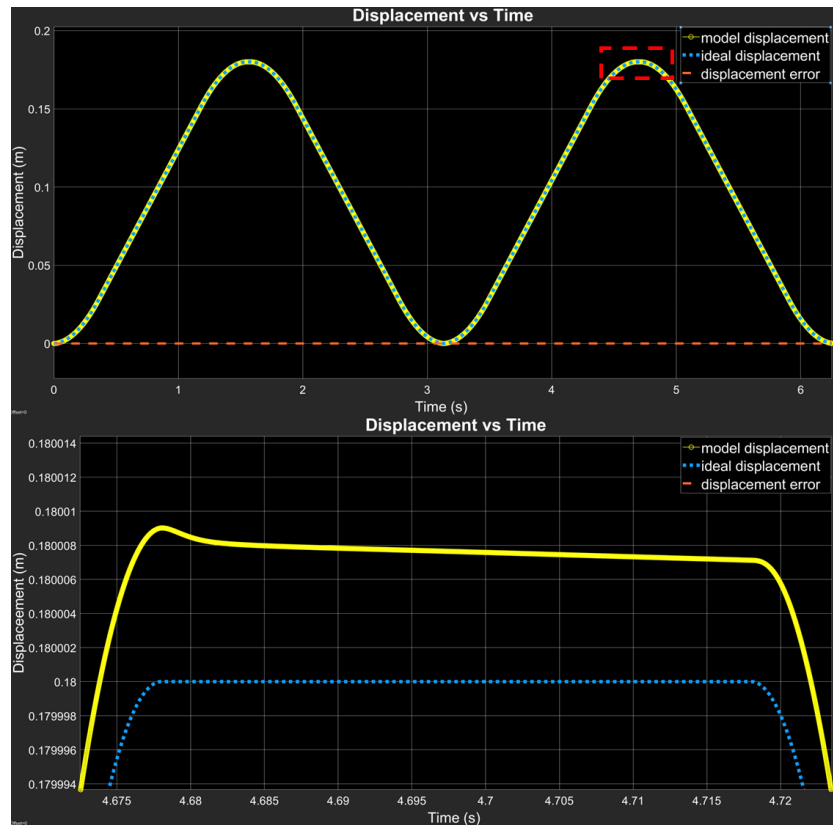


Figure 14: Displacement plot for ideal and dynamic model for Test 3 parameters (above) and zoomed plot of rectangular region (below)

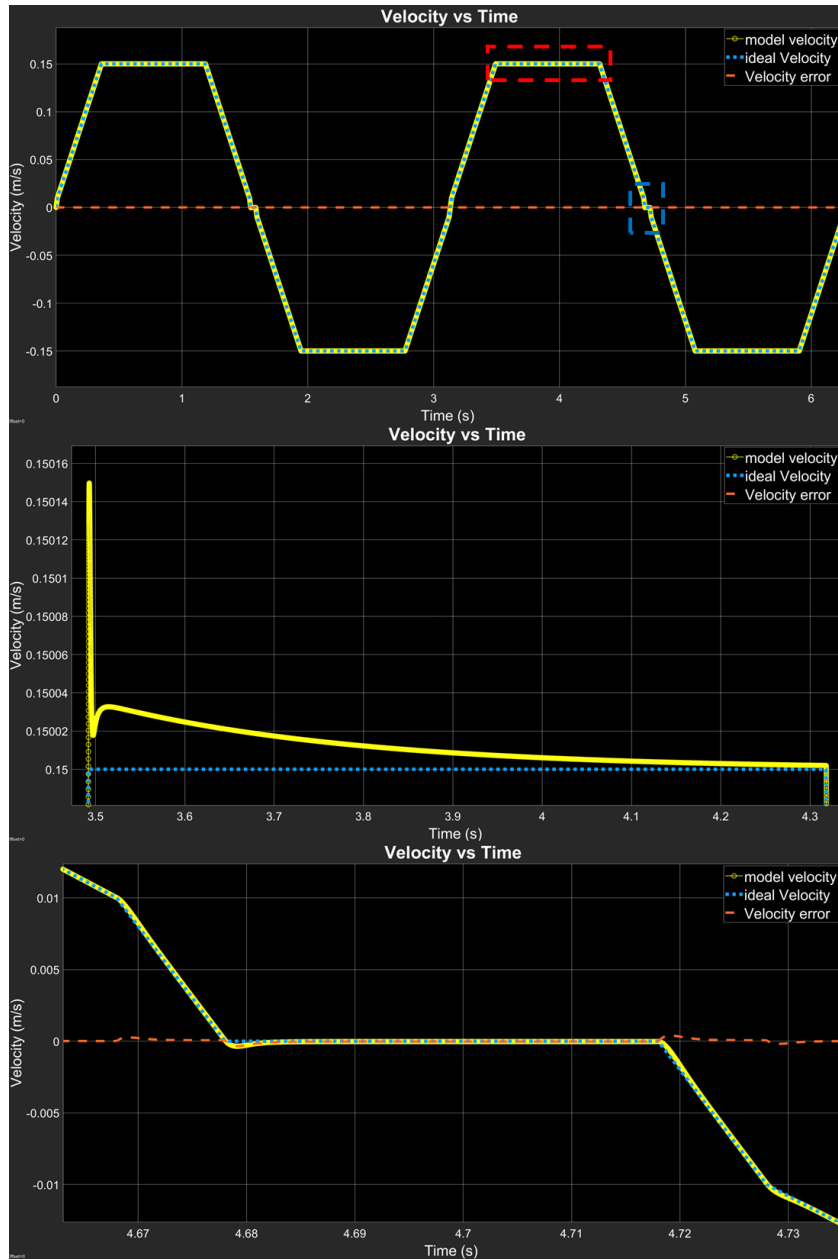


Figure 15: Velocity plot for ideal and dynamic model for Test 3 parameters (above), zoomed plot of red rectangular region (middle) and zoomed plot of blue rectangular region (bottom)

Table 8 presents the peak displacement of the extruder carriage for all the models with their respective test parameters from Table 5 and their corresponding errors. The error between the experimental model and the dynamic model is less than the error between the experimental and ideal model. The average error between the dynamic and experimental model is 0.27 mm, while the average error between the experimental and ideal model is 0.31 mm. Therefore, the presented dynamic model gives a better prediction about the position of the extruder carriage system as compared to the ideal model.

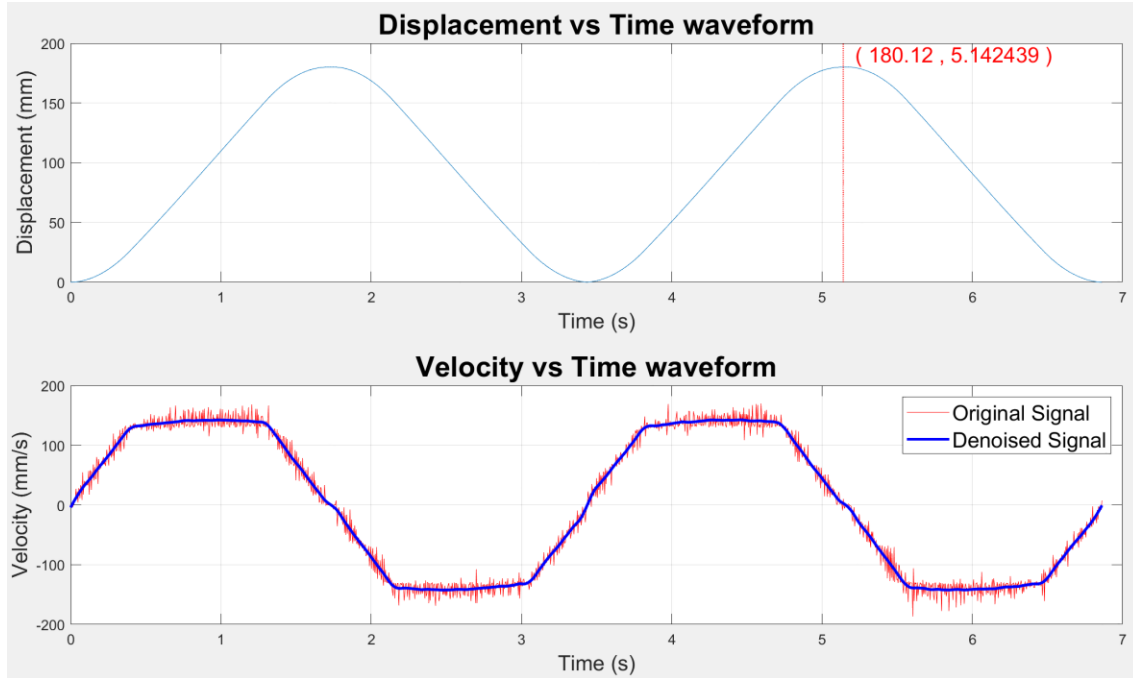


Figure 16: Displacement (above) and velocity (below) plot for Test 3 experiment

Table 7: Pixel data for different heights

Height category	Distance	Pixels
0-1 mm	180	590.72
50-51 mm	180	643.56
100-101 mm	180	620.65
150-151 mm	180	559.87

Although the experimental data has a few irregularities owing to the setup and vision tracking, the error is more consistent with the variation in the same height category. For instance, tests 2, 5, 12, and 15 are at the same height between 50-51 mm and have errors towards the higher side. In the same way, tests 4, 7, 10 and 13 have the same height between 150-151 mm and have error towards the lower category. The major reason for this error is mostly due to the vision system tracking related to pixel sensitivity (Table 7) and partly due to the change in stiffness in k_3 and vibration. Since the camera used captures wide angle views, the pixels captured are not uniform. The trend is towards higher pixels for higher error as can be seen from Table 7 and 8. If the errors from tests between height 50-51 mm are ignored, the average error between the dynamic and experimental model is only 0.1 mm compared to 0.12 mm. Thus, the dynamic model can represent the position of the carriage more accurately almost in the order of 0.1 mm. Highly precise tracking systems can give more practical results and identify the true position value of the extruder carriage.

Table 8: Peak displacement of the models and associated error

Test	Displacement Ideal (mm) (A)	Displacement Dynamic (mm) (B)	Displacement Experiment (mm) (C)	Error (mm) (C-A)	Error (mm) (C-B)
1	180	180.03	180.23	0.23	0.2
2	180	180.04	180.89	0.89	0.85
3	180	180.05	180.12	0.12	0.07
4	180	180.05	180.02	0.02	0.03
5	180	180.04	180.85	0.85	0.81
6	180	180.04	180.31	0.31	0.27
7	180	180.05	180.07	0.07	0.02
8	180	180.06	180.05	0.05	0.01
9	180	180.03	180.07	0.07	0.04
10	180	180.04	179.96	0.04	0.08
11	180	180.05	180.16	0.16	0.11
12	180	180.06	180.84	0.84	0.78
13	180	180.03	179.95	0.05	0.08
14	180	180.04	180.06	0.06	0.02
15	180	180.05	180.84	0.84	0.79
16	180	180.06	180.29	0.29	0.23

4. Predictive Control Concepts

Predictive control is a feed-forward control used in systems when the system dynamics are well-known and can be predicted. The state-space equations provided earlier form the basis for implementing control system. In the previous section, it is shown that the presented dynamic model of the 3D printer can accurately predict the extruder carriage position in mid-range to high speeds. Implementing predictive control requires very less modification of the system such that the dynamic equations governing the system are almost the same with some minor additions. The main advantage of using predictive control is that it is easier to implement, requires smaller investment, and does not limit the printing speed. Predictive control with passive elements has the potential to reduce end position errors in printing. A spring-mass-damper system or an inverted pendulum can be used to minimize printing errors. To implement predictive control, the passive control system dynamic equations are added to the state-space equation with appropriate values. The state-space equations of the complete system will be of the form

$$\dot{X} = (A + P)X + (B + Q)u \quad (49)$$

4.1. Spring-Mass-Damper Example

A spring-mass-damper system can be attached to the extruder carriage top surface as a passive control co-design (Figure 17). When the extruder carriage moves, the system moves along with it, while having its own motion. To find the effect the spring-mass-damper on the carriage motion, the dynamic equations must be derived. Here force F is the force applied to the extruder carriage by the printer system which has been calculated earlier and shown in Eq 12. The dynamic equations of motion for this system can be derived as:

$$\ddot{x}_6 = -\frac{k_7}{m_{6t}}x_4 + \frac{k_7}{m_{6t}}x_7 - \frac{\beta_7}{m_{6t}}\dot{x}_4 + \frac{\beta_7}{m_{6t}}\dot{x}_7 + \frac{F}{m_{6t}} \quad (50)$$

$$\ddot{x}_7 = \frac{k_7}{m_7}x_4 - \frac{k_7}{m_7}x_7 + \frac{\beta_7}{m_7}\dot{x}_4 - \frac{\beta_7}{m_7}\dot{x}_7 \quad (51)$$

Note that m_{6t} is the mass of the extruder carriage and the mass of the spring-mass-damper system. These equations can be directly added to the system equations derived for the full system state-space equations. The resulting state space equation will have 2 additional states.

$$[z_1 z_2 z_3 z_4 z_5 z_6 z_7 z_8 z_9 z_{10} z_{11} z_{12} z_{13} z_{14}] = [x_1 \dot{x}_1 x_2 \dot{x}_2 x_3 \dot{x}_3 x_4 \dot{x}_4 \theta_4 \dot{\theta}_4 \theta_5 \dot{\theta}_5 x_7 \dot{x}_7] \quad (52)$$

The state-space equation can be added in the form of Eq 49 to get the complete state-space equations for the dynamic model. It is clear that there is no significant change in the overall dynamics of the system. In equation 49, since there is no additional input force to the system, $Q=0$. The values of the mass, spring constant and the damping coefficient must be calculated using simulations to find the appropriate values to reduce end position error while making sure that the extruder carriage does not undershoot or overshoot.

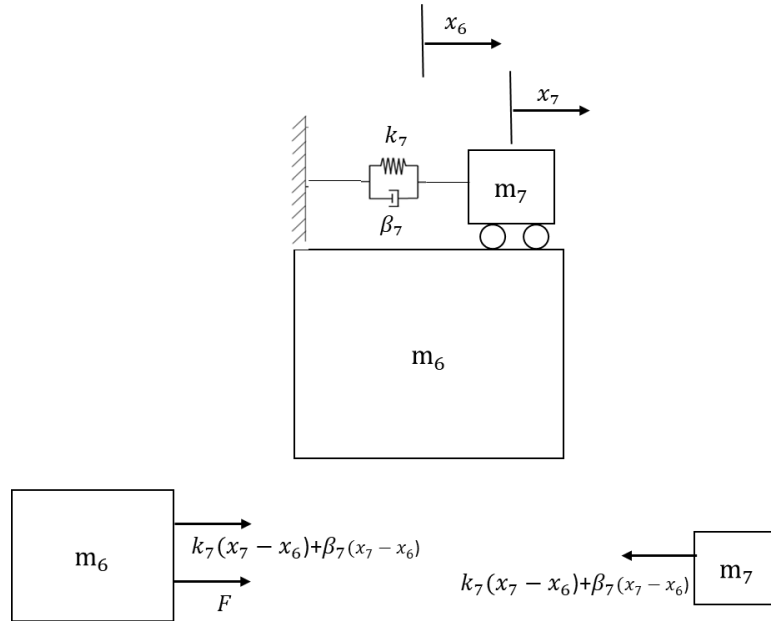


Figure 17: Spring-mass-damper system on the extruder carriage with free-body diagram

4.2. Inverted Pendulum with Rotational Spring Example

In this example an inverted pendulum with a rotational spring is mounted on top of the extruder carriage (Figure 18). The pendulum can rotate on top and its movement is dependent on gravity and motion of the extruder carriage. At the junction of the pendulum rod and the carriage there is a rotational spring of stiffness k_7 (N/rad) trying to keep the pendulum at vertical position. It is assumed that the spring force is acting against the rotation of the pendulum and has no effect in the horizontal motion of the extruder carriage. Thus, the extruder carriage motion is independent of the rotational spring force. The dynamic equation of the system will be derived first, and the effect of the rotational spring will be added at the end. Force F is applied to the extruder carriage by the printer system which has already been calculated.

It is assumed that the pendulum does not rotate much and the value of θ_7 is small compared to the displacement. This can be assumed due to the presence of the rotational spring. Mass of the pendulum is concentrated

at the center of the pendulum, assuming the mass of the rod is negligible. The linear acceleration of the extruder carriage is found to be

$$\ddot{x}_4 = \frac{F}{m_4} - \frac{m_4 g \theta_7}{m_7} \quad (53)$$

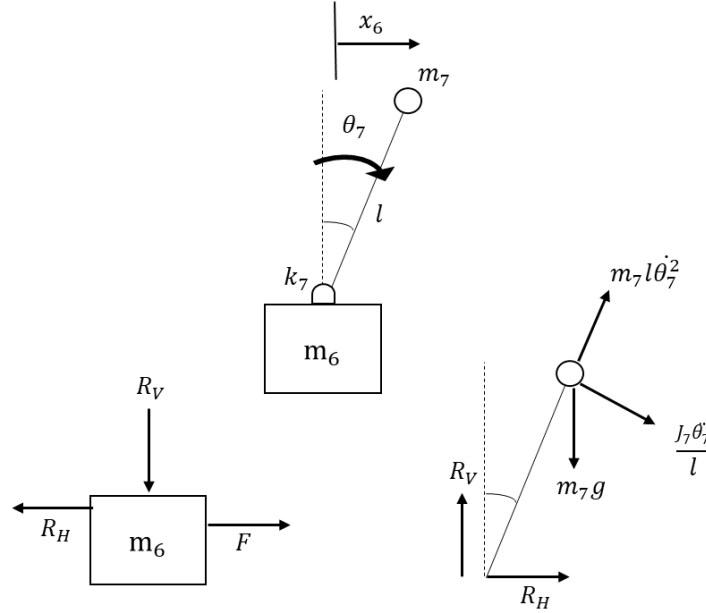


Figure 18: Inverted pendulum system with a rotational spring on the extruder carriage

And the angular acceleration of the pendulum is found is

$$\ddot{\theta}_7 = \frac{(m_4 + m_7)g\theta_7}{m_4 l} - \frac{F}{m_4 l} + \frac{k_7 \theta_7}{m_4 l} \quad (54)$$

Eq 53 and 54 can be added to the state space equation of the system derived earlier. Similar to the spring-mass-damper system, 2 state variables will be added to the system θ_7 and $\dot{\theta}_7$. In the case of the inverted pendulum, the effect of gravitational force is present in the equations of motion for both extruder and pendulum. This external force was not present in the spring-mass-damper system. Appropriate pendulum mass and length of the rod must be calculated by simulating the dynamic model such that the extruder carriage travels the required length. This step must be completed before implementing the system physically in the printer.

5. Conclusions and Future Work

The dynamic model of a cartesian-frame FFF 3D printer has been presented in this study. The non-conservative and non-linear dynamic model of the extruder carriage system follows closely with the physical printer in study. The position of the carriage can be precisely determined with a high level of accuracy up to 0.1 mm. This shows that the dynamic model presented in this study is promising and can be further developed to determine the motion of the extruder carriage. The conservative dynamic model presented has been verified using both Newton-Euler based force method and Lagrange's energy method, validating the mathematical dynamic equations for the model. Modelling of FFF 3D printer has high potential to reduce printing and machine related errors, especially errors related to end position. Although the models will vary from printer to printer, Prusa frame printer users can use this model to estimate the extruder carriage position. Using the dynamic model, passive control elements can be introduced into the system to reduce printing errors by predictive control. The examples presented in this study can be modelled to calculate the parameters of the passive control elements and can be implemented in the physical system to study its effects and reduce end position errors; producing higher quality parts at higher speeds and reducing cost of production.

The model can also be used for feedback control as understanding and modelling of the system is paramount to both control methods.

Acknowledgements

The authors thank Dr. James Allison for discussion and advice on formulation and dynamic modeling in this problem. While this publication represents a complete re-derivation and re-formulation of unpublished earlier work, the authors recognize Dr. Allison's contributions to the motivation and research approach on this problem.

Raw Data and Code

All raw data and code for this work are available upon request to the authors.

References

1. Messimer, S.L., Patterson, A.E., Muna, N., et al (2018). Characterization and Processing Behavior of Heated Aluminum-Polycarbonate Composite Build Plated for the FDM additive Manufacturing Process.
2. Anzalone, G.C., Wijnen, B., & Pearce, J.M. (2015). Multi-material additive and subtractive prosumer digital fabrication with a free and open-source convertible delta RepRap 3-D printer. *Rapid Prototyping Journal*, 21(5): 506-519.
3. Nuchitprasitchai, S., Roggemann, M.C., & Pearce, J.M. (2017). Three Hundred and Sixty Degree Real-Time Monitoring of 3-D Printing Using Computer Analysis of Two Camera Views. *Journal of Manufacturing and Materials Processing*, 1(2): 2.
4. Irwin, J.L., Pearce, J.M., Anzalone, G., Opplinger, D.E. (2014). The RepRap 3-D Printer Revolution in STEM Education. *Proceedings of the 121st ASEE Annual Conference and Exposition, Indianapolis, IN, June 15-18, 2014*: Paper # 8696.
5. Ishak, I., Fisher, J., & Larochelle, P. (2016). Robotic Arm for Additive Manufacturing: Multi-Lane Printing. *Proceedings of the 29th Florida Conference on Recent Advances in Robotics, Miami, FL, May 12-13, 2016*: 146-151.
6. Keating, S. & Oxman, N. (2013). Compound fabrication: A multi-functional robotic platform for digital design and fabrication. *Robotics and Computer-Integrated Manufacturing*, 29(6): 439-448.
7. Raghavan, A., Neethu, P.P., & Joy, A. (2017). 3D Printing Robotic Arm. *International Journal of Engineering and Management Research*, 7(3): 631-634.
8. Li, X., Lian, Q., Li, D., et al. (2017). Development of a Robotic Arm Based Hydrogel Additive Manufacturing System for In-Situ Printing. *Applied Sciences*, 7(1): 73.
9. Pierrot, F., Reynaud, C., & Fournier, A. (1990). DELTA: a simple and efficient parallel robot. *Robotica*, 8: 105-109.
10. Stock, M. & Miller, K. (2003). Optimal Kinematic Design of Spatial Manipulators: Application to Linear Delta Robot. *Journal of Mechanical Design*, 125: 292-301.
11. Bell, C. (2015). "Delta Printer Hardware" In C. Bell, *3D Printing with Delta Printers* (pp. 39-70). New York, NY: Apress (Springer-Nature).
12. Arena, J.D. & Allison, J.T. (2014). Solving the Reconfigurable Design Problem for Multiability with Applications to Robotic Systems. *Proceedings of 2014 ASME International Design Engineering Technical Conference, Buffalo, NY, August 17-20, 2014*: Paper # DETC2014-35314.
13. Arena, J.D. (2014). *Design Considerations for a Reconfigurable Delta Robot* (M.S. Thesis). University of Illinois at Urbana-Champaign, Urbana, Illinois, USA. Available online: <http://systemdesign.illinois.edu/publications/Are14a.pdf>.
14. Graves, S. (2013). Johann C. Rocholl (Rostock) Style Delta Robot Kinematics (Technical Report). Available online at http://www.reprap.org/mediawiki/images/b/b5/Rostock_Delta_Kinematics_3.pdf.
15. Pearce, J.M. (2015). Applications of Open Source 3-D Printing on Small Farms. *Organic Farming*, 1(1): 19-35.
16. Patterson, A. E., Chadha, C., and Jasiuk, I. M., 2021, "Identification and Mapping of Manufacturability Constraints for Extrusion-based Additive Manufacturing", *Journal of Manufacturing and Materials Processing*, 5(2), p. 33.
17. Altintas, Y. & Khoshdarregi, M.R. (2012). Contour error control of CNC machine tools with vibration avoidance. *CIRP Annals – Manufacturing Technology*, 61: 335-338.
18. Khim, G., Park, C.H., Shamoto, E., et al. (2011). Prediction and compensation of motion accuracy in a linear motion bearing table. *Precision Engineering*, 35: 393-399.
19. Schmitz, T.L., Ziegert, J.C., Canning, J.S., et al. (2008). Case study: A comparison of error sources in high-speed milling. *Precision Engineering*, 32: 126-133.
20. Messimer, S., Pereira, T., Patterson, A., Lubna, M., and Drozda, F., 2019, "Full-density Fused Deposition Modeling Dimensional Error as a Function of Raster Angle and Build Orientation: Large Dataset for Eleven Materials", *Journal of Manufacturing and Materials Processing*, 3(1), p. 6.
21. Lanzotti, A., Del Giudice, D.M., Lepore, A., et al. (2015). On the Geometric Accuracy of RepRap Open-Source Three-Dimensional Printer. *Journal of Mechanical Design*, 137: 101703.

22. Lanzotti, A., Martorelli, M., & Staiano, G. (2015). Understanding Process Parameter Effects of RepRap Open-Source Three-Dimensional Printers Through a Design of Experiments Approach. *Journal of Manufacturing Science and Engineering*, 137: 011017.
23. Pilch, Z., Domin, J., & Szlapa, A. (2015). The impact of vibration of the 3D printer table on the quality of the print. *Proceedings of Selected Problems of Electrical Engineering and Electronics Conference (WZEE), 17-19 September 2015, Kielce, Poland*.
24. Ahn, D., Kim, H., & Lee, S. (2009). Surface roughness prediction using measured data and interpolation in layered manufacturing. *Journal of Materials Processing Technology*, 209: 664-671.
25. Patterson, A.E., Chadha, C., Jasiuk, I.M. and Allison, J.T. (2023). Tensile behavior of individual fibers and films made via material extrusion additive manufacturing. *Next Materials*, 1(1), p.100002.
26. Ahn, D., Kweon, J-H., Kwon, S., et al. (2009). Representation of surface roughness in fused deposition modeling. *Journal of Materials Processing Technology*, 209: 5593-5600.
27. Armillotta, A. (2006). Assessment of surface quality on textured FDM prototypes. *Rapid Prototyping Journal*, 12(1): 35-41.
28. Baumann, F.W., Eichhoff, J.R., & Roller, D. (2017). Scanned Image Data from 3-D Printed Specimens Using Fused Deposition Modeling. *Data*, 2(1): 3.
29. Boschetto, A., Giordano, V., & Veniali, F. (2013). 3D roughness profile model in fused deposition modelling. *Rapid Prototyping Journal*, 19(4): 240-252.
30. Patterson, A.E., Chadha, C., Jasiuk, I.M. and Allison, J.T. (2021). Fracture testing of polymer materials processed via fused filament fabrication: a survey of materials, methods, and design applications. *Progress in Additive Manufacturing*, 6(4), pp.765-780.
31. Andersson, S., Soderberg, A., & Bjorklund, S. (2007). Friction models for sliding dry, boundary and mixed lubricated contacts. *Tribology International*, 40: 580-587.
32. Behzad, M., Bastami, A.R., & Mba, D. (2011). A New Model for Estimating Vibrations Generated in the Defective Rolling Element Bearings. *Journal of Vibrations and Acoustics*, 133: 041011.
33. Cao, H., Niu, L., Xi, S., et al. (2018). Mechanical model development of rolling bearing-rotor systems: A review. *Mechanical Systems and Signal Processing*, 102: 37-58.
34. Dietmair, A. & Verl, A. (2009). Drive Based Vibration Reduction for Production Machines. *Modern Machinery Science Journal*, 3(4): 130-134.
35. Fujii, Y. (2004). An optical method for evaluating frictional characteristics of linear bearings. *Optics and Lasers in Engineering*, 42: 493-501.
36. Fujii, Y., Maru, K., Jin, T., et al. (2010). A Method for Evaluating Dynamical Friction in Linear Ball Bearings. *Sensors*, 10: 10069-10080.
37. Fujii, Y. & Maru, K. (2010). Optical Method for Evaluating Dynamic Friction of a Small Linear Ball Bearing. *Tribology Transactions*, 53: 169-173.
38. *SDP/SI Handbook of Timing Belts, Pulleys, Chains, and Sprockets*. Available online: www.sdp-si.com/PDFS/Technical-Section-Timing.pdf. Accessed November 15, 2017.
39. Widnall, S. (2009). *Energy Methods: Lagrange's Equations*. Published lecture notes, *Massachusetts Institute of Technology*, Fall 2009. Available online: https://ocw.mit.edu/courses/aeronautics-and-astronautics/16-07-dynamics-fall-2009/lecture-notes/MIT16_07F09_Lec20.pdf. Accessed January 30, 2018.
40. The Engineering Toolbox. Available online: https://www.engineeringtoolbox.com/rolling-friction-resistance-d_1303.html. Accessed March 27, 2023.
41. Shangquan, W-B. & Zeng, Z-K. (2013). Modeling and Validation of Rotational Vibration Responses for Accessory Drive Systems – Part I: Experiments and Belt Modeling. *Journal of Vibration and Acoustics*, 135: 031002.
42. Hunt, J.F., Zhang, H., Guo, Z., & Fu, F. (2013). Cantilever Beam Static and Dynamic Response Comparison with Mid-Pont Bending for Thin MDF Composite Panels. *BioResources*, 8(1): 115-129.
43. Liu, W. (2008). *Experimental and Analytical Estimation of Damping in Beams and Plates with Damping Treatments*. Doctoral dissertation, University of Kansas.
44. Perez-Pena, A., Garcia-Granada, A.A., Menacho, J., et al. (2016). A methodology for damping measurement of engineering materials: application to a structure under bending and torsional load. *Journal of Vibration and Control*, 22(10): 2471-2481.
45. Wang, B., Si, Y., et al. (2018). Nominal Stiffness of GT-2 Rubber-Fiberglass Timing Belts for Dynamic System Modeling and Design. *Robotics* 7(4),75. <https://doi.org/10.3390/robotics7040075>.
46. Jones, D.W. (2004). *Microchip Technologies Technical Manual: Stepping Motor Fundamentals*. Publication AN907. Available online: <http://www.microchip.com/wwwAppNotes/AppNotes.aspx?appnote=en012151>. Accessed February 2, 2018.
47. Hopkins, T. (2010). Stepper Motor Controller/Driver Simplifies Stepper Motor System. *Power Electronics Technology*, August 2010: 24-27.
48. Baluta, G. (2007). Microstepping Model for Stepper Motor Control. *Proceedings of 2007 IEEE Conference on Signals, Circuits, and Systems (ISSCS 2007), July 13-14, 2017, Iasi, Romania*: 1-4.
49. Shamith, L.S., Arivarsai, A., & Anand, K.R. (2016). Design of a Stepper Motor for Nano Resolution 3D Printing. *Proceedings of 2016 World Congress on Engineering and Computer Science (WCECS), October 19-21, San Francisco, USA*: 280-285.

50. Rahman, M., Schott, N.R., & Sadhu, L.K. (2016). Glass Transition of ABS in 3D Printing. *Proceedings of the 2016 Boston COMSOL Conference, October 5-7, Boston, USA.*
51. Jerez-Mesa, R., Travieso-Rodriguez, J.A., Corbella, X., et al. (2016). Finite element analysis of the thermal behavior of a RepRap 3D printer liquefier. *Mechatronics*, 36: 119-126.